


# Intensity enhancement of Raman active and forbidden modes induced by naturally occurred hot spot at GaAs edge

Tao Liu(刘涛), Miao-Ling Lin(林妙玲), Da Meng(孟达), Xin Cong(从鑫), Qiang Kan(阚强), Jiang-Bin Wu(吴江滨), and Ping-Heng Tan(谭平恒)

**Citation:**Chin. Phys. B, 2025, 34 (**1**): 017801. DOI: 10.1088/1674-1056/ad9ff9

**What follows is a list of articles you may be interested in**

---

## Investigation of reflection anisotropy induced by micropipe defects on the surface of a 4H-SiC single crystal using scanning anisotropy microscopy

Wei Huang(黄威), Jinling Yu(俞金玲), Yu Liu(刘雨), Yan Peng(彭燕),Lijun Wang(王利军), Ping Liang(梁平), Tangsheng Chen(陈堂胜), Xiangang Xu(徐现刚), Fengqi Liu(刘峰奇), and Yonghai Chen(陈涌海)

Chin. Phys. B, 2024, 33 (**3**): 037801. DOI: 10.1088/1674-1056/acf27f

## Elemental composition x-ray fluorescence analysis with a TES-based high-resolution x-ray spectrometer

Bingjun Wu(吴秉骏), Jingkai Xia(夏经铠), Shuo Zhang(张硕), Qiang Fu(傅强), Hui Zhang(章辉),Xiaoming Xie(谢晓明), and Zhi Liu(刘志)

Chin. Phys. B, 2023, 32 (**9**): 097801. DOI: 10.1088/1674-1056/acd926

## A pure dielectric metamaterial absorber with broadband and thin thickness based on a cross-hole array structure

Wenbo Cao(曹文博), Youquan Wen(温又铨), Chao Jiang(姜超), Yantao Yu(余延涛), Yiyu Wang(王艺宇), Zheyipei Ma(麻哲乂培), Zixiang Zhao(赵子翔), Lanzhi Wang(王兰志), and Xiaozhong Huang(黄小忠)

Chin. Phys. B, 2022, 31 (**11**): 117801. DOI: 10.1088/1674-1056/ac6492

## A novel natural surface-enhanced fluorescence system based on reed leaf as substrate for crystal violet trace detection

Hui-Ju Cao(曹会菊), Hong-Wen Cao(曹红文), Yue Li(李月), Zhen Sun(孙祯), Yun-Fan Yang(杨云帆), Ti-Feng Jiao(焦体峰), and Ming-Li Wang(王明利)

Chin. Phys. B, 2022, 31 (**10**): 107801. DOI: 10.1088/1674-1056/ac7215

## Different angle-resolved polarization configurations of Raman spectroscopy: A case on the basal and edge plane of two-dimensional materials

Xue-Lu Liu(刘雪璐), Xin Zhang(张昕), Miao-Ling Lin(林妙玲), Ping-Heng Tan(谭平恒)

Chin. Phys. B, 2017, 26 (**6**): 067802. DOI: 10.1088/1674-1056/26/6/067802

---

**RAPID COMMUNICATION**

# Intensity enhancement of Raman active and forbidden modes induced by naturally occurred hot spot at GaAs edge

Tao Liu(刘涛)[1,2], Miao-Ling Lin(林妙玲)[1,2], Da Meng(孟达)[1,2], Xin Cong(从鑫)[1,2], Qiang Kan(阚强)[2,3], Jiang-Bin Wu(吴江滨)[1,2], and Ping-Heng Tan(谭平恒)[1,2,†]

[1] *State Key Laboratory of Semiconductor Physics and Chip Technologies, Institute of Semiconductors, Chinese Academy of Sciences, Beijing* 100083, *China*
[2] *Center of Materials Science and Optoelectronics Engineering, University of Chinese Academy of Sciences, Beijing* 100049, *China*
[3] *Key Laboratory of Optoelectronic Materials and Devices, Institute of Semiconductors, Chinese Academy of Sciences, Beijing* 100083, *China*

(Received 16 October 2024; revised manuscript received 14 December 2024; accepted manuscript online 17 December 2024)

Edge structures are ubiquitous in the processing and fabrication of various optoelectronic devices. Novel physical properties and enhanced light–matter interactions are anticipated to occur at crystal edges due to the broken spatial translational symmetry. However, the intensity of first-order Raman scattering at crystal edges has been rarely explored, although the mechanical stress and edge characteristics have been thoroughly studied by the Raman peak shift and the spectral features of the edge-related Raman modes. Here, by taking GaAs crystal with a well-defined edge as an example, we reveal the intensity enhancement of Raman-active modes and the emergence of Raman-forbidden modes under specific polarization configurations at the edge. This is attributed to the presence of a hot spot at the edge due to the redistributed electromagnetic fields and electromagnetic wave propagations of incident laser and Raman signal near the edge, which are confirmed by the finite-difference time-domain simulations. Spatially-resolved Raman intensities of both Raman-active and Raman-forbidden modes near the edge are calculated based on the redistributed electromagnetic fields, which quantitatively reproduce the corresponding experimental results. These findings offer new insights into the intensity enhancement of Raman scattering at crystal edges and present a new avenue to manipulate light–matter interactions of crystal by manufacturing various types of edges and to characterize the edge structures in photonic and optoelectronic devices.

**Keywords:** polarized Raman spectroscopy, edge, enhanced Raman scattering, spatial translational symmetry breaking, electromagnetic field redistribution, finite-difference time-domain simulation

**PACS:** 78.30.–j, 13.88.+e, 42.25.Gy, 47.20.Ky

**DOI:** 10.1088/1674-1056/ad9ff9 **CSTR:** 32038.14.CPB.ad9ff9

## 1. Introduction

Edge structure, a special defect with broken spatial translational symmetry, is prevalent in integrated circuits and optoelectronic devices and has garnered significant attention due to the unique physical properties emerging at the edges of advanced materials. Notable phenomena such as half-metal[1] and magnetic responses[2,3] have been observed in graphene nanoribbons. Additionally, quantum spin Hall states have been detected at the edges of 1T′-$WTe_2$,[4] and enhanced nonlinear optical resonances were observed at the edges of $MoS_2$.[5] A deeper understanding of these edge-specific properties could profoundly advance the design of artificial structures for next-generation optical devices.[6–8]

Raman spectroscopy, a widely used technique for probing light–matter interactions and phonon-related physical properties,[9] has been instrumental in studying various materials.[10–13] In particular, Raman spectroscopy provides valuable insights into edge structures. For example, local mechanical stress at crystal edges, which modifies the lattice structure and alters the phonon distribution, has been probed through Raman peak shifts.[14–17] A further detailed study on the emergence of edge-related modes (e.g., D mode in graphene) and its spectral feature can be used to characterize the edge orientations, edge types and the alignment configuration at edges.[18–20] In addition, hot spot can form due to the redistribution of electromagnetic field at crystal edges with spatial translational symmetry breaking.[21] Therefore, Raman signal is expected to be modified at crystal edges. Surface-enhanced Raman scattering has been fully explored thanks to the local electromagnetic field confinement at the interfaces between two media with broken spatial translational symmetry.[22–26] However, despite the observed intensity enhancement[27,28] at the edges in silicon-based devices and the violation of Raman selection rules at the edges of several two-dimensional materials,[29–32] there is still a lack of a comprehensive understanding of these experimental phenomena and the corresponding physical mechanism.

In this study, by using GaAs crystal with a well-defined edge as a model system, we reveal the intensity enhancement of Raman-active modes and the emergence of Raman-forbidden modes at the edge under specific polarization con-

†Corresponding author. E-mail: phtan@semi.ac.cn

© 2025 Chinese Physical Society and IOP Publishing Ltd. All rights, including for text and data mining, AI training, and similar technologies, are reserved.

figurations. The finite-difference time-domain (FDTD) simulation shows that the presence of a hot spot at the edge results from the electromagnetic field redistribution dependent on laser polarization. The corresponding simulated results can well reproduce the experimental Raman intensity near the edge as functions of position, wavelength of excitation laser and numerical aperture (NA) of objectives.

## 2. Experimental setup and theoretical method

### 2.1. Sample preparation

The GaAs wafer oriented along the (1 1 0) plane was washed with acetone and ethanol to remove iodine adsorbed on the surface. Then, the wafer was scratched with a glass cutter and manually broken to create a well-defined edge, which was further confirmed by optical microscope.

### 2.2. Raman measurements

Raman measurements were performed in a backscattering geometry using a Jobin-Yvon HR800 system equipped with a liquid-nitrogen-cooled charge-coupled detector. Raman spectra were collected at room temperature using a 100× objective lens with NA = 0.90, as well as 50× and 20× long-working-distance objectives with NA values of 0.55 and 0.25, respectively. The excitation wavelengths ($\lambda_{ex}$) are 532 nm from a solid-state laser, 488 nm from an $Ar^+$ laser, and 442 nm from a He–Cd laser. A 1800 lines/mm grating was employed. The step size for line-scan Raman imaging is 0.2 μm. A polarizer and a half-wave plate were placed in the incident path to change the polarization direction of the incident laser. A half-wave plate and an analyzer were located before the spectrometer entrance to change the polarization direction of the Raman signal. By rotating the two half-wave plates, the polarization directions of the incident laser and Raman signal can be aligned along the $x$ or $y$ axis of the GaAs crystal, denoted as $X$ or $Y$ polarizations, respectively, which enables four polarization configurations: $XX$, $XY$, $YX$, and $YY$, where the first letter indicates the polarization direction of the incident laser and the last letter indicates that of the Raman signal. For accuracy, Raman intensity was obtained from the Raman peak area in this study.

### 2.3. FDTD simulation

The FDTD simulations were conducted using Max Optics Studio, developed by Shanghai Max-Optics Information Technology Co., Ltd. The simulation area covered 10 μm in the $x$ and $y$ directions ($-5$ μm $\le x \le 5$ μm, and $-5$ μm $\le y \le 5$ μm) and 1.6 μm in the $z$ direction ($-1$ μm $\le z \le 0.6$ μm). The edge of the GaAs wafer was positioned at $x = 0$ and $z = 0$. The refractive indexes of GaAs were referenced from Ref. [33] and the simulation thickness of GaAs exceeded the penetration depth of the three lasers. The numbers of mesh cells were 1000, 500, and 50 in the $x$, $y$, and $z$ directions, respectively. Perfectly matched layers were placed around the simulated area as the boundary conditions for FDTD simulations. The incident laser was modeled as a Gaussian beam propagating along the $z$ direction, with polarizations along the $x$ or $y$ axis. The Gaussian beam waists were 3.79 μm, 0.96 μm, and 0.36 μm for $\lambda_{ex}$ of 532 nm, corresponding to the measured spot sizes for the objective with NAs of 0.25, 0.55, and 0.90, respectively. The focus spot of the incident laser was set on the $z = 0$ plane. To simulate the line-scan Raman imaging, the focus spot of the incident laser was moved from $x < 0$ to $x > 0$ with a step size of 0.02 μm near the GaAs edge.

## 3. Results and discussion

For a general Raman scattering, the Raman intensity of a crystal measured from the basal plane can be described by the following Raman selection rule:

$$I \propto \omega_s^4 \int |\boldsymbol{e}_s \cdot \boldsymbol{F}_s \cdot \boldsymbol{R} \cdot \boldsymbol{F}_i \cdot \boldsymbol{e}_i|^2 \mathrm{d}V, \tag{1}$$

where $\omega_s$ represents the photon frequency of Raman signals, $\boldsymbol{R}$ is the Raman tensor of a phonon mode, $V$ is the effective volume illuminated by the incident laser, and $\boldsymbol{e}_i$ ($\boldsymbol{e}_s$) and $\boldsymbol{F}_i$ ($\boldsymbol{F}_s$) denote the unit vectors and electromagnetic field distribution of the incident laser (Raman signal), respectively. For a Gaussian laser beam, $\boldsymbol{F}_i = F_0 \exp(\frac{-r^2}{w^2})\boldsymbol{I}_3$, $\boldsymbol{F}_s = \boldsymbol{I}_3$, where $F_0$ is the initial electromagnetic field amplitude, $r$ represents the radial distance from the center axis of the laser beam, $w$ is the waist radius of the Gaussian laser beam and $\boldsymbol{I}_3$ denotes the $3 \times 3$ identity matrix. The Raman intensity is sensitive to the laser spot position near the edge due to the change of the effective volume illuminated by the incident laser.

To gain a fundamental understanding of Raman scattering at the edge, we employed the experimental configuration shown in Fig. 1(a). Both the incident laser and Raman signal can be polarized along the $x$ axis ($\boldsymbol{e}_i = \boldsymbol{e}_s^T = (1\ 0\ 0)^T$) or the $y$ axis ($\boldsymbol{e}_i = \boldsymbol{e}_s^T = (0\ 1\ 0)^T$), resulting in four possible polarization Raman configurations: $XX$, $XY$, $YY$ and $YX$. The corresponding Raman intensities are denoted as $I_{XX}$, $I_{XY}$, $I_{YY}$, and $I_{YX}$, respectively. As shown in Fig. 1(b), the well-defined edge of GaAs(1 1 0) surface is parallel to the $y$ axis. The Raman spectra at the basal plane and the edge under the $YY$ configuration are presented in Fig. 1(c), showing two characteristic Raman peaks corresponding to the transverse optical (TO) mode at $\sim 268$ cm$^{-1}$ and the longitudinal optical (LO) mode at $\sim 292$ cm$^{-1}$. The Raman tensor of these two modes for GaAs(1 1 0) are[34]

$$R(\mathrm{TO}) = \frac{1}{\sqrt{2}}\begin{pmatrix} 0 & 0 & d \\ 0 & 0 & d \\ d & d & 0 \end{pmatrix}, \quad \frac{1}{\sqrt{2}}\begin{pmatrix} 0 & 0 & d \\ 0 & 0 & -d \\ d & -d & 0 \end{pmatrix},$$

$$R(\mathrm{LO}) = \begin{pmatrix} e & 0 & 0 \\ 0 & -e & 0 \\ 0 & 0 & 0 \end{pmatrix}, \tag{2}$$

where $d$ and $e$ are constants. According to Eq. (1), $I_{XX}(\mathrm{LO}) = I_{YY}(\mathrm{LO}) = \omega_s^4 d^2 F_0^2 \int \exp(\frac{-2r^2}{w^2}) \mathrm{d}V$, $I_{XY}(\mathrm{LO}) = I_{YX}(\mathrm{LO}) = 0$, and $I_{XX}(\mathrm{TO}) = I_{YY}(\mathrm{TO}) = I_{XY}(\mathrm{TO}) = I_{YX}(\mathrm{TO}) = 0$. As depicted in Fig. 1(c), the TO mode is nearly forbidden under $YY$ configuration at the basal plane. However, the strong TO mode at the GaAs edge cannot be understood by the general Raman selection rule. To further investigate the differences between the Raman signals at the edge and the basal plane, we performed line-scan Raman imaging near the edge under four polarization configurations, as shown in Fig. 1(d). The laser spot position ($x$) was moved from $x = -5$ μm to $x = 5$ μm, where $x < 0$ μm corresponds to air, and $x > 0$ μm represents GaAs. At the basal plane ($x = 2$ μm), Raman intensities of the LO and TO modes follow the general selection rule: the LO mode is allowed under $YY$ and $XX$ configurations but forbidden under $YX$ and $XY$ configurations, while the TO mode is forbidden under all the configurations. However, the case at the edge ($x = 0$ μm) is significantly different. As the laser spot approaches the edge from the basal plane, $I_{XX}(\mathrm{LO})$ and $I_{YY}(\mathrm{LO})$ gradually decrease, while $I_{XY}(\mathrm{LO})$ and $I_{YX}(\mathrm{LO})$ remain zero. Notably, $I_{XX}(\mathrm{LO})$ at $x = 0$ μm is almost half as strong as that at $x = 2$ μm due to the decrease of the effective volume illuminated by the incident laser, while $I_{YY}(\mathrm{LO})$ at $x = 0$ μm remains similar to that at $x = 2$ μm. Furthermore, the TO modes appear at the edge under all four configurations. The enhancement of Raman-active LO modes and the emergence of Raman-forbidden TO modes imply a redistribution of electromagnetic fields at the edge.

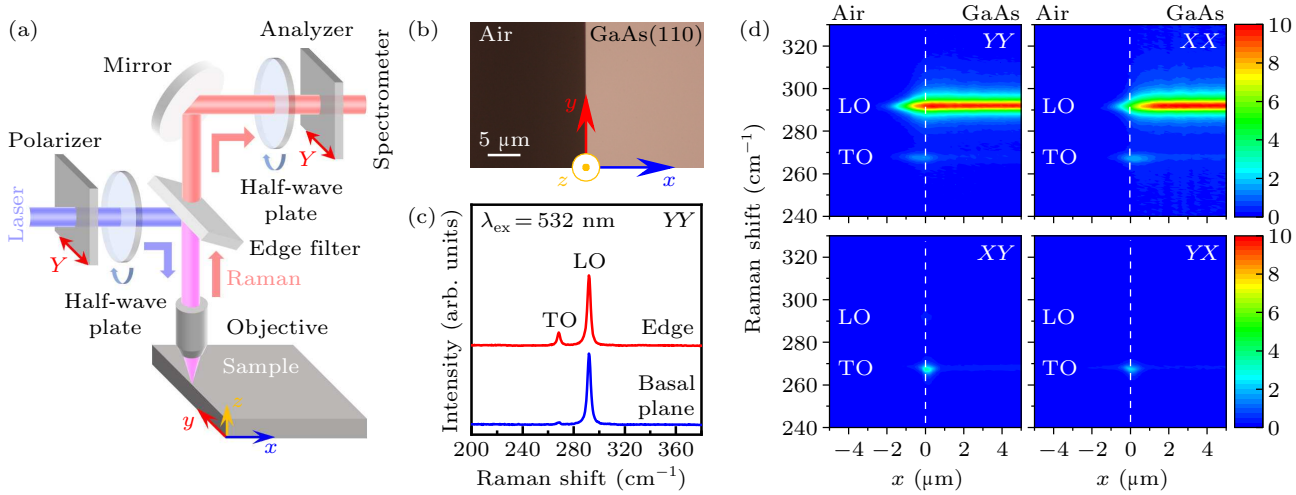



**Fig. 1.** (a) Schematic of the polarization-resolved Raman spectroscopy setup. (b) Optical image of GaAs(1 1 0) crystal with a well-defined edge parallel to the $y$ axis. (c) Raman spectra at the basal plane and the edge under the $YY$ polarization configuration. (d) Line-scan Raman imaging under four different polarization configurations (i.e., $YY$, $XX$, $XY$ and $YX$). $\lambda_{ex} = 532$ nm and NA = 0.90.

We constructed an FDTD model to show the propagation of incident laser at the edge and the basal plane in time domain, as depicted in Fig. 2. Figures 2(a) and 2(b) show the distribution of the incident laser ($\lambda_{ex} = 532$ nm and NA = 0.90) over time for the $Y$- and $X$-polarizations (i.e., $E_Y$ and $E_X$), respectively. The modulus square of electromagnetic field ($|E_m|^2$, $m = Y, X$) in the $x$–$z$ plane was obtained by integrating the corresponding ones along the $y$ axis. For $E_Y$ in Fig. 2(a), the electromagnetic field of the incident laser at the edge and the basal plane propagated vertically at 8 fs, with the laser focus positioned at the air/GaAs interface. At 16 fs, the distribution of electromagnetic field near the air/GaAs interface exhibited notable differences between the edge and the basal plane. At the basal plane, the electromagnetic field continued to propagate vertically, with part of it transmitting into the GaAs. In contrast, at the edge, the electromagnetic field no longer propagated vertically but underwent significant redistribution, forming a hot spot. At 22 fs, the electromagnetic field was nearly zero in the simulation region. The behavior of $E_X$ in Fig. 2(b) was quite similar to $E_Y$ in Fig. 2(a), except that the distribution of $E_X$ differed significantly from $E_Y$ near the edge at 16 fs. Additionally, the modulus square of electromagnetic field at the hot spot of $E_X$ within the GaAs was weaker than that of $E_Y$.

To further demonstrate the distribution of different components of electromagnetic field clearly, we also transformed the simulation results into the frequency domain at both the edge and the basal plane, as shown in Fig. 3. The modulus square of electromagnetic field components ($|E_m^n|^2$, $n = X, Y, Z$, $m = Y, X$) in the $x$–$z$ plane was obtained by integrating the corresponding ones along the $y$ axis. For the components of $E_Y$ in Fig. 3(a), the $|E_Y^X|^2$ and $|E_Y^Z|^2$ were nearly zero at the basal plane, while $|E_Y^Y|^2$ showed appreciable values and followed a Gaussian distribution. However, at the edge, $|E_Y^Y|^2$, and $|E_Y^Z|^2$ showed significant values. $|E_Y^Z|^2$ was relatively small inside the GaAs crystal, whereas $|E_Y^Y|^2$ was substantially enhanced

at the edge, showing a significant hot spot, and its distribution deviated notably from a Gaussian distribution. For the components of $E_X$ in Fig. 3(b), the case at the basal plane was quite similar to that of $E_Y$. The $|E_X^X|^2$ displayed a Gaussian distribution, while $|E_X^Y|^2$ and $|E_X^Z|^2$ were nearly zero. At the edge, $|E_X^X|^2$ inside the GaAs was also enhanced, although its magnitude was much smaller compared to $|E_Y^Y|^2$. A notable change at the edge for the components of $E_X$ was the much larger value of $|E_X^Z|^2$ compared with $|E_Y^Z|^2$, especially inside the GaAs. These results demonstrate that the broken spatial translational symmetry at the edge can significantly modulate the distribution of the electromagnetic field components and promote the formation of the hot spot. Additionally, the difference in $|E_m^n|^2$ at the edge between the $X$ and $Y$ polarizations suggests that the modulation introduced by the broken spatial translational symmetry is dependent on the polarization of the incident laser, consistent with previous reports in the literature.[27–29]

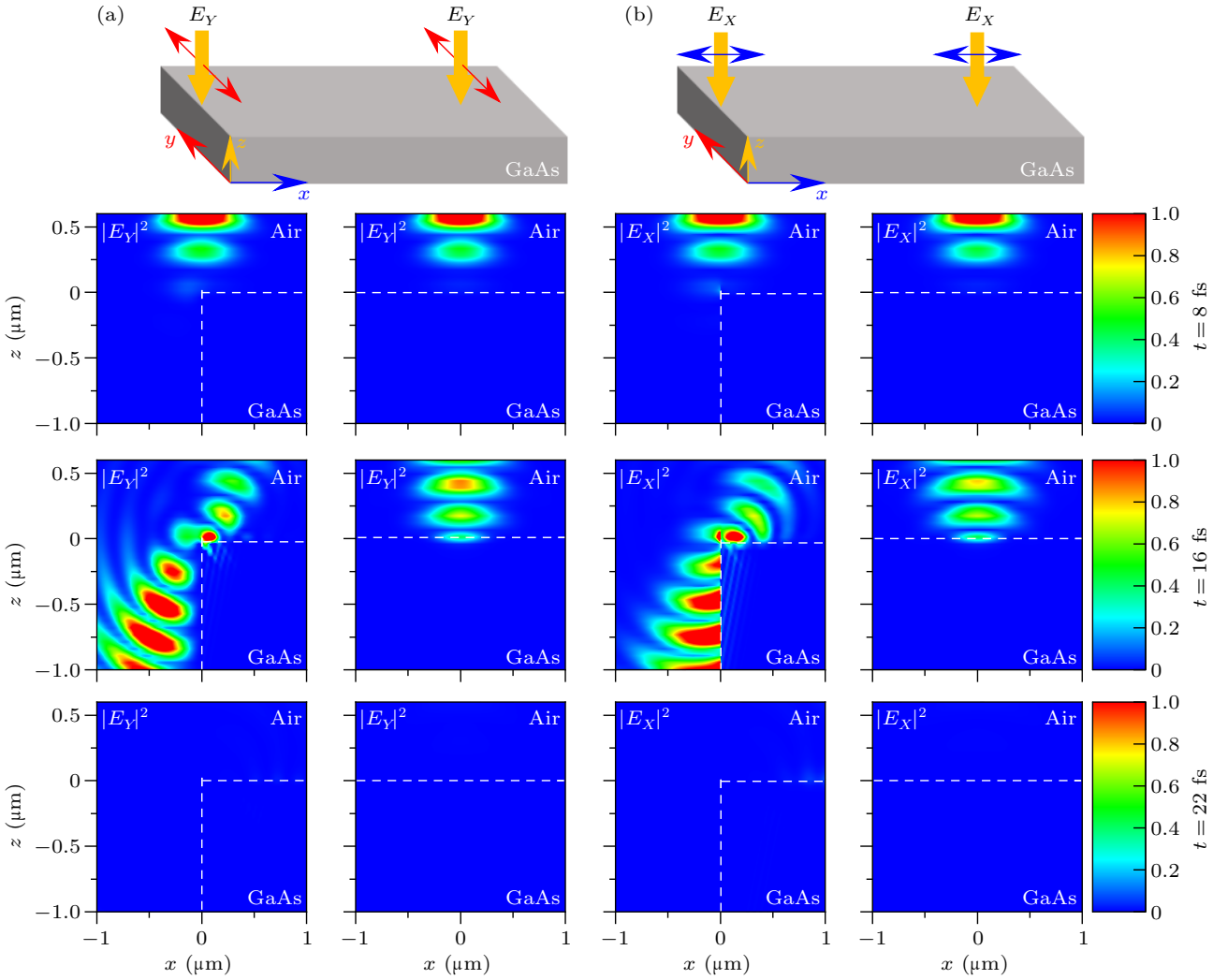



**Fig. 2.** Modulus square of total electromagnetic field ($|E_m|^2$, $m = Y, X$) at the edge and the basal plane for (a) $Y$- and (b) $X$-polarized incident lasers. $\lambda_{ex} = 532$ nm and NA = 0.90.

To calculate Raman intensity induced by the redistribution of the electromagnetic fields at the hot spot near the edge, we should formulate the corresponding $\boldsymbol{F}_i$ and $\boldsymbol{F}_s$ in Eq. (1). In this case, $\boldsymbol{F}_i$ is no longer a diagonal matrix and the element in $\boldsymbol{F}_i$ is equal to the corresponding component $E_m^n$ ($m = X, Y$ and $n = X, Y$ and $Z$) shown in Fig. 3. Similar to the previous studies,[35–37] we assume that the enhancement of Raman signal is of the same magnitude as that of the incident laser and the nondiagonal element in the matrix $\boldsymbol{F}_s$ can be ignored. Furthermore, the diagonal element in the matrix $\boldsymbol{F}_s$ is equal to the corresponding element in electromagnetic field vector, i.e., $\boldsymbol{F}_s^{ii} = (\boldsymbol{R} \cdot \boldsymbol{F}_i \cdot \boldsymbol{e}_i)^i$. Consequently, the Raman scattering signal should be proportional to the fourth power of the amplitudes of the involved electromagnetic field component.[35–37] Under $YY$ and $XX$ polarization Raman configurations, the corresponding total Raman intensities should be $I_{YY}^{tot}(\mathrm{LO}) \propto \omega_s^4 e^2 \int |E_Y^Y|^4 \mathrm{d}V$ and $I_{XX}^{tot}(\mathrm{LO}) \propto \omega_s^4 e^2 \int |E_X^X|^4 \mathrm{d}V$, while under the $YX$ and $XY$ polarization Raman configurations, the relevant electromagnetic field component of the LO mode $E_X^Y$ and $E_Y^X$ is nearly zero, respectively, as shown in Fig. 3. Consequently, $I_{YX}^{tot}(\mathrm{LO}) = I_{XY}^{tot}(\mathrm{LO}) = 0$ at the edge, consistent with the results presented in Fig. 1(d).

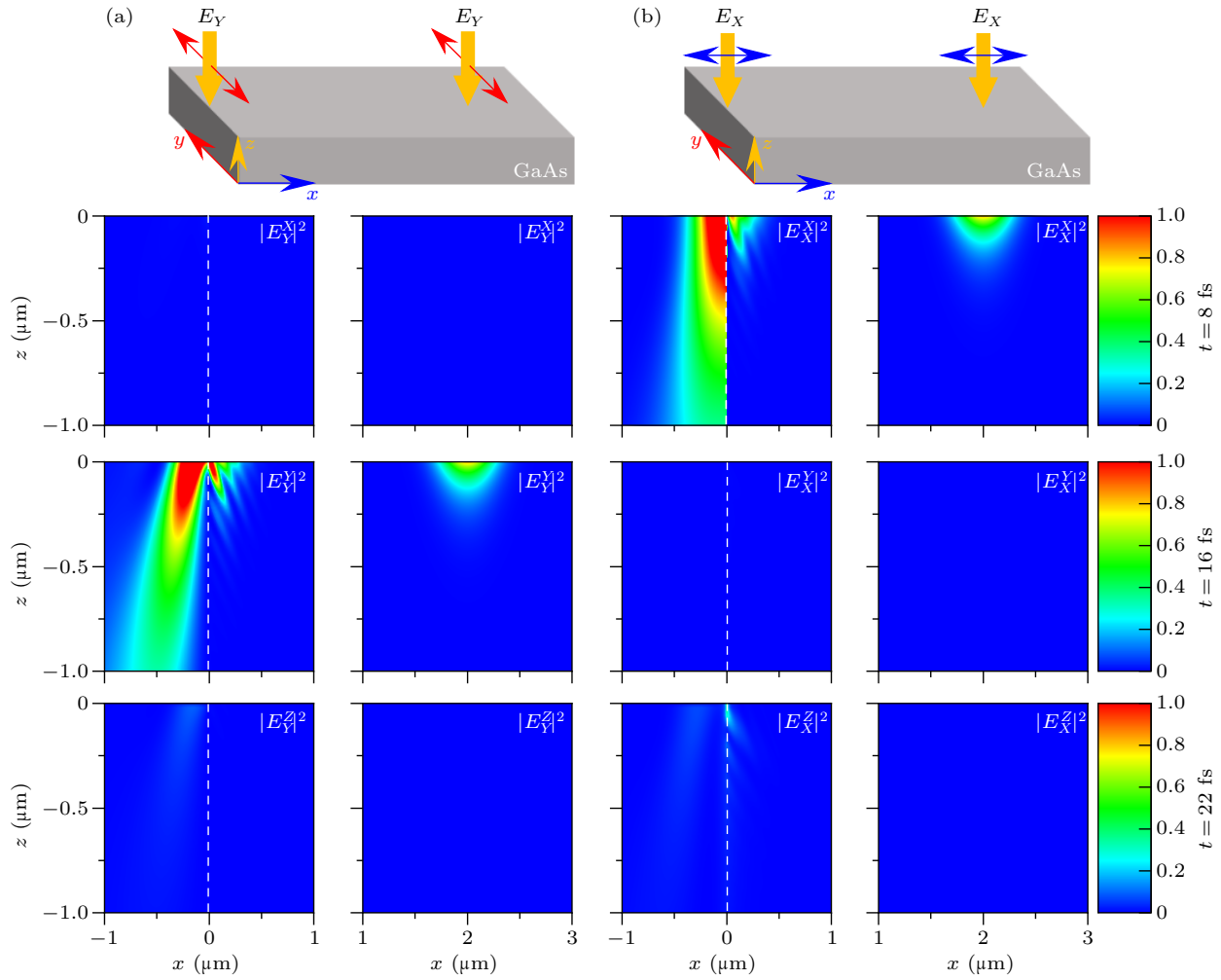



**Fig. 3.** Modulus square of electromagnetic field components ($|E_m^n|^2$, $n = X, Y, Z$, $m = Y, X$) at the edge and at the basal plane for (a) $Y$- and (b) $X$-polarized incident lasers. $\lambda_{ex} = 532$ nm and NA = 0.90.

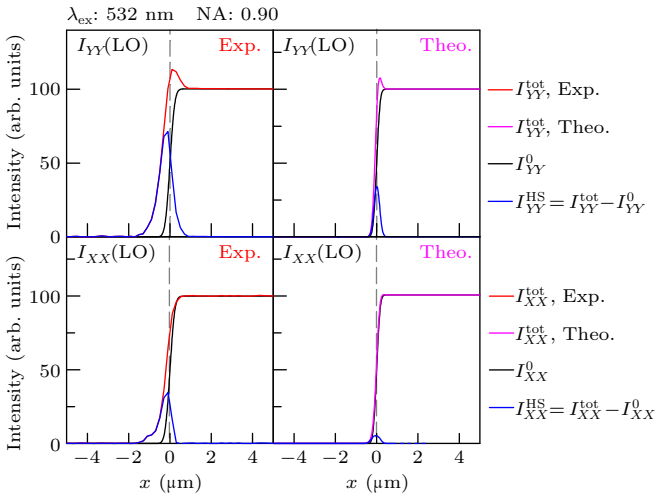



**Fig. 4.** Experimental (Exp., red lines) and theoretical (Theo., pink lines) $I_{YY}^{tot}$(LO) ($I_{XX}^{tot}$(LO)) as functions of $x$. Both $I_{YY}^0$(LO) and $I_{XX}^0$(LO) are indicated by black lines, and both $I_{YY}^{HS}$(LO) and $I_{XX}^{HS}$(LO) are indicated by blue lines. $\lambda_{ex} = 532$ nm and NA = 0.90.

Figure 4 presents the experimental intensities (red lines) of the LO mode extracted from Fig. 1(d) and the theoretical intensities (pink lines) of the LO mode calculated using Eq. (1) with the simulated $|E_m^n|^2$ in Fig. 3 near the edge. The measured experimental $I_{YY}^{tot}$(LO) increases as $x$ increases from negative to positive, reaching a maximum at $x \simeq 0.1$ μm and then $I_{YY}^{tot}$(LO) decreases to a constant value as $x$ becomes larger than 2 μm. In contrast, the measured experimental $I_{XX}^{tot}$(LO) increases to a constant as $x$ increases from negative to positive without exhibiting a maximum near the edge. The theoretical $I_{YY}^{tot}$(LO) and $I_{XX}^{tot}$(LO) are similar to the experimental ones.

To figure out the intrinsic Raman intensity ($I^{HS}$) enhancement induced by the hot spot at the GaAs edge, we calculated $I_{YY}^0$(LO) and $I_{XX}^0$(LO) (black lines) via Eq. (1) during the line scan, where the superscript 0 represents that the electromagnetic field of incident laser follows a Gaussian distribution inside GaAs and the hot spot is not considered at GaAs edge. The corresponding intensities (blue lines) induced by the hot spot at GaAs edge can be obtained, i.e., $I_{YY}^{HS}(\mathrm{LO}) = I_{YY}^{tot}(\mathrm{LO}) - I_{YY}^0(\mathrm{LO})$ and $I_{XX}^{HS}(\mathrm{LO}) = I_{XX}^{tot}(\mathrm{LO}) - I_{XX}^0(\mathrm{LO})$. In order to directly compare the theoretical results between $I^{tot}$ and $I^0$, $\boldsymbol{F}_s$ in theoretical $I_{XX}^0$(LO) ($I_{YY}^0$(LO)) still satisfies the assumptions mentioned above and the theoretical $I^0$ is assumed to be proportional to the fourth power of the amplitudes of the involved electromagnetic field component. The

experimental and theoretical $I_{YY}^{\mathrm{HS}}(\mathrm{LO})$ and $I_{XX}^{\mathrm{HS}}(\mathrm{LO})$ reach their maxima at the edge for both polarization configurations, quantitatively demonstrating the enhancement effect of the edge on Raman intensity. The maximum $I_{XX}^{\mathrm{HS}}(\mathrm{LO})$ is smaller than that of $I_{YY}^{\mathrm{HS}}(\mathrm{LO})$, further highlighting that the modulation of the electromagnetic field redistribution at the hot spot is dependent on the polarization of the incident laser. Notably, the full widths at half maximum (FWHM) of the theoretical $I_{YY}^{\mathrm{HS}}(\mathrm{LO})$ and $I_{XX}^{\mathrm{HS}}(\mathrm{LO})$ are approximately half that of the corresponding experimental ones. This difference is attributed to the fact that the theoretical intensity is proportional to $|E_m^n|^4$ across all $x$, whereas in experiments, the laser and Raman signals are both enhanced simultaneously only when the laser is positioned at the hot spot near edge. In fact, when $x$ is slightly away from the hot spot near edge, the experimental intensity is proportional to $|E_m^n|^2$.

To gain a deeper understanding of the influence of edge structure on Raman intensity, we conducted line-scan Raman imaging experiments on the GaAs sample using different $\lambda_{\mathrm{ex}}$ and objectives with different NAs. Figure 5(a) shows the $I_{YY}^{\mathrm{HS}}(\mathrm{LO})$ and $I_{XX}^{\mathrm{HS}}(\mathrm{LO})$ as functions of $x$, using an objective with a 0.90 NA at $\lambda_{\mathrm{ex}} = 532$ nm (green lines), 488 nm (blue lines) and 442 nm (purple lines). According to Eq. (1), the Raman intensity is approximately proportional to the fourth power of the excitation frequency. Furthermore, charge-coupled device efficiencies are also dependent on $\lambda_{\mathrm{ex}}$. To eliminate these factors dependent on $\lambda_{\mathrm{ex}}$, the intensity of the $A_1$ mode at $\sim 207$ cm$^{-1}$ from quartz samples was used as a reference for normalization. The maximum $I_{YY}^{\mathrm{HS}}(\mathrm{LO})$ and $I_{XX}^{\mathrm{HS}}(\mathrm{LO})$ decrease as $\lambda_{\mathrm{ex}}$ becomes shorter. This phenomenon results from the fact that the incident laser with shorter wavelengths is absorbed more significantly inside GaAs crystal, leading to a reduced scattering volume within the crystal. Notably, the maximum $I_{YY}^{\mathrm{HS}}(\mathrm{LO})$ decreases more quickly with shorter wavelengths than that of $I_{XX}^{\mathrm{HS}}(\mathrm{LO})$, suggesting that the enhanced electromagnetic fields at the edge are concentrated near the top surface when the incident laser is $X$-polarized. The $I_{YY}^{\mathrm{HS}}(\mathrm{LO})$ and $I_{XX}^{\mathrm{HS}}(\mathrm{LO})$ also vary with the NA of objectives at $\lambda_{\mathrm{ex}} = 532$ nm as shown in Fig. 5(b). The green, blue, and purple lines represent $I_{YY}^{\mathrm{HS}}(\mathrm{LO})$ and $I_{XX}^{\mathrm{HS}}(\mathrm{LO})$ with objectives of NA = 0.90, 0.55, and 0.25, respectively. The experimental and theoretical results show reasonable agreement. As the NA decreases, the power density of the incident laser at the focus diminishes and thus the Raman intensities at the edge should decrease with decreasing NA, as shown by the sharp decline in $I_{YY}^{\mathrm{HS}}(\mathrm{LO})$ and $I_{XX}^{\mathrm{HS}}(\mathrm{LO})$.

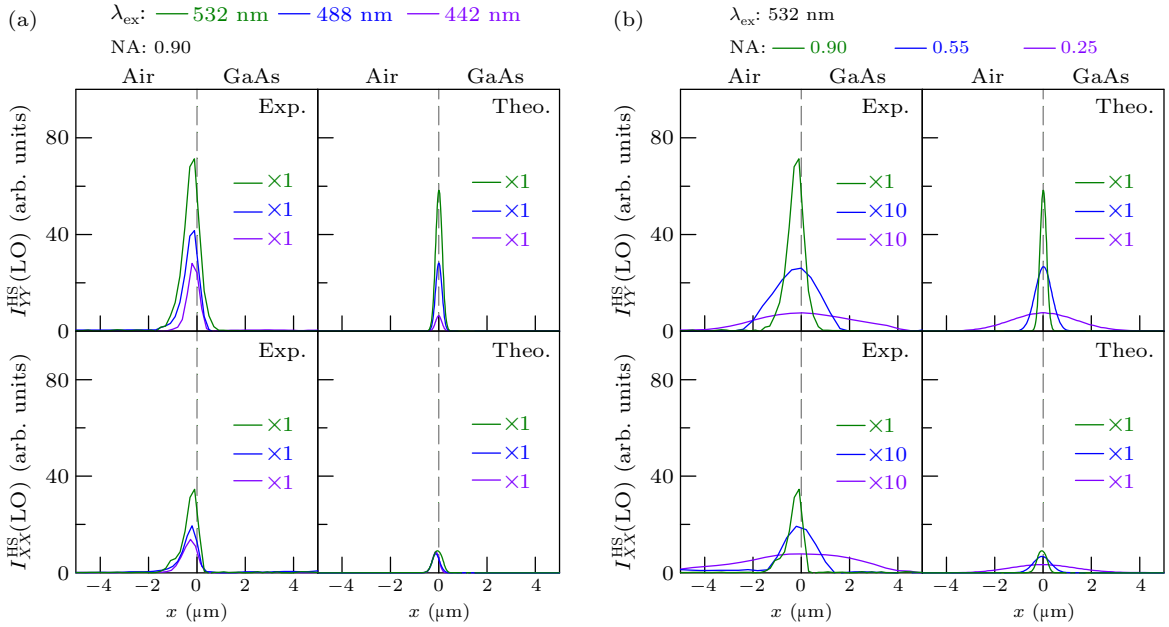



**Fig. 5.** Experimental (Exp.) and theoretical (Theo.) $I_{YY}^{\mathrm{HS}}(\mathrm{LO})$ and $I_{XX}^{\mathrm{HS}}(\mathrm{LO})$ as functions of $x$. (a) $\lambda_{\mathrm{ex}} = 532$ nm (green lines), 488 nm (blue lines) and 442 nm (purple lines), NA = 0.90; (b) $\lambda_{\mathrm{ex}} = 532$ nm, NA = 0.90 (green lines), 0.55 (blue lines) and 0.25 (purple lines).

In addition to the enhanced Raman intensity of the LO mode, the redistribution of the electromagnetic field components at the edge also leads to the observation of the forbidden TO mode in the Raman spectra from the edge, as shown in Figs. 1(c) and 1(d). According to Eq. (1), the Raman intensities of the TO mode at the hot spot near the edge can be expressed as $I_{YY}^{\mathrm{tot}}(\mathrm{TO}) \propto \omega_{\mathrm{s}}^4 d^2 \int |E_Y^Z|^4 \mathrm{d}V$, $I_{YX}^{\mathrm{tot}}(\mathrm{TO}) \propto \omega_{\mathrm{s}}^4 d^2 \int |E_Y^Z|^4 \mathrm{d}V$, $I_{XX}^{\mathrm{tot}}(\mathrm{TO}) \propto \omega_{\mathrm{s}}^4 d^2 \int |E_X^Z|^4 \mathrm{d}V$ and $I_{XY}^{\mathrm{tot}}(\mathrm{TO}) \propto \omega_{\mathrm{s}}^4 d^2 \int |E_X^Z|^4 \mathrm{d}V$. Figures 6(a) and 6(b) show the corresponding $I_{YY}^{\mathrm{HS}}(\mathrm{TO})$, $I_{YX}^{\mathrm{HS}}(\mathrm{TO})$, $I_{XX}^{\mathrm{HS}}(\mathrm{TO})$ and $I_{XY}^{\mathrm{HS}}(\mathrm{TO})$ as functions of $x$ excited by $\lambda_{\mathrm{ex}} = 532$ nm (green lines), 488 nm (blue lines) and 442 nm (purple lines), under parallel ($YY$, $XX$) and cross ($YX$, $XY$) polarization configurations and NA = 0.90, respectively. Experimental data and theoretical results reach their maxima at $x = 0$ μm in both Figs. 6(a) and 6(b), highlighting the enhancement by the hot spot due to edge-induced translational

symmetry breaking. Similar to the LO mode, the corresponding intensities of the TO mode also decrease with shorter $\lambda_{ex}$, attributed to the reduced penetration depth. However, unlike the LO mode, the corresponding intensities of the TO mode decrease at a similar rate with shorter wavelengths for both $X$- and $Y$-polarized incident lasers. This indicates that $E_Y^Z$ and $E_X^Z$ are not concentrated near the top surface.

Figures 7(a) and 7(b) show NA-dependent $I_{YY}^{HS}(TO)$, $I_{YX}^{HS}(TO)$, $I_{XX}^{HS}(TO)$ and $I_{XY}^{HS}(TO)$ at $\lambda_{ex} = 532$ nm under parallel ($YY$, $XX$) and cross ($YX$, $XY$) polarization configurations, respectively. As NA decreases, the corresponding intensity profiles of the TO mode show larger FWHM due to the larger laser spot size. A smaller NA also leads to a lower power density, which reduces the modulus square of $E_Y^Z$ ($E_X^Z$) component and causes a decline in the maximum intensities. Furthermore, a smaller NA results in a less convergent Gaussian laser, leading to a weaker $Z$-polarized component. For the TO mode, the profiles of experimental and theoretical intensities show good agreement. However, the absolute theoretical intensities $I_{YY}^{HS}(TO)$ and $I_{YX}^{HS}(TO)$ differ significantly from the corresponding experimental data. This discrepancy can be partially attributed to limitations in accurately simulating the Gaussian beam for Raman scattering, and potential differences in the enhancement of electromagnetic field components between the Raman scattered signal and the incident laser.

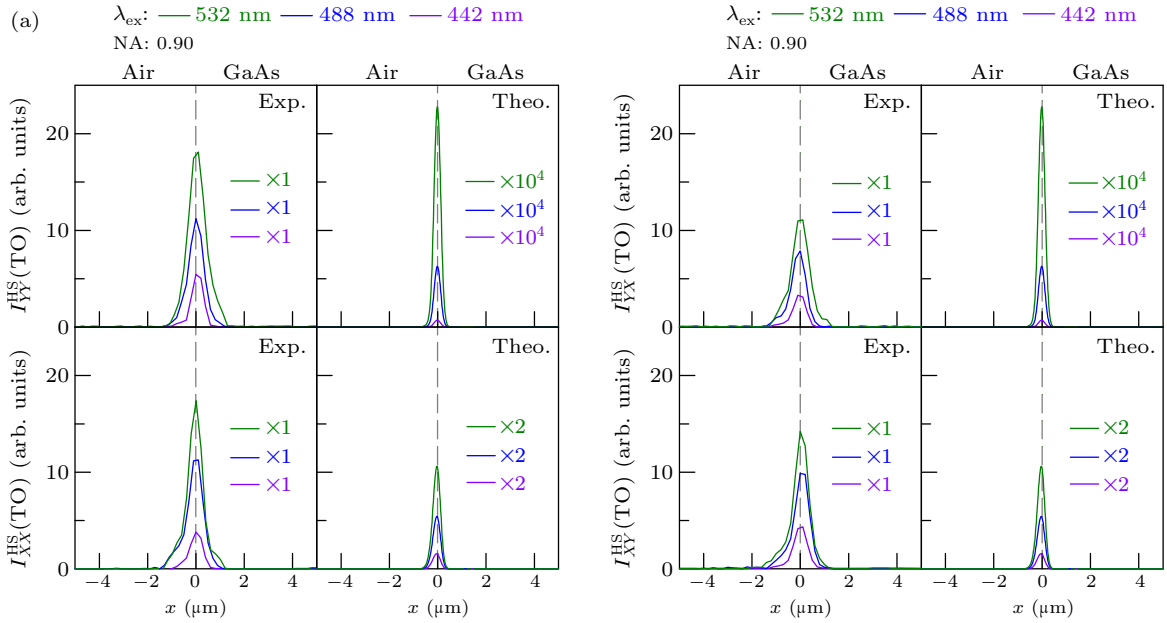



**Fig. 6.** Experimental (Exp.) and theoretical (Theo.) (a) $I_{YY}^{HS}(TO)$ and $I_{XX}^{HS}(TO)$, and (b) $I_{YX}^{HS}(TO)$ and $I_{XY}^{HS}(TO)$ as functions of $x$ excited by $\lambda_{ex} = 532$ nm (green lines), 488 nm (blue lines) and 442 nm (purple lines), NA = 0.90.

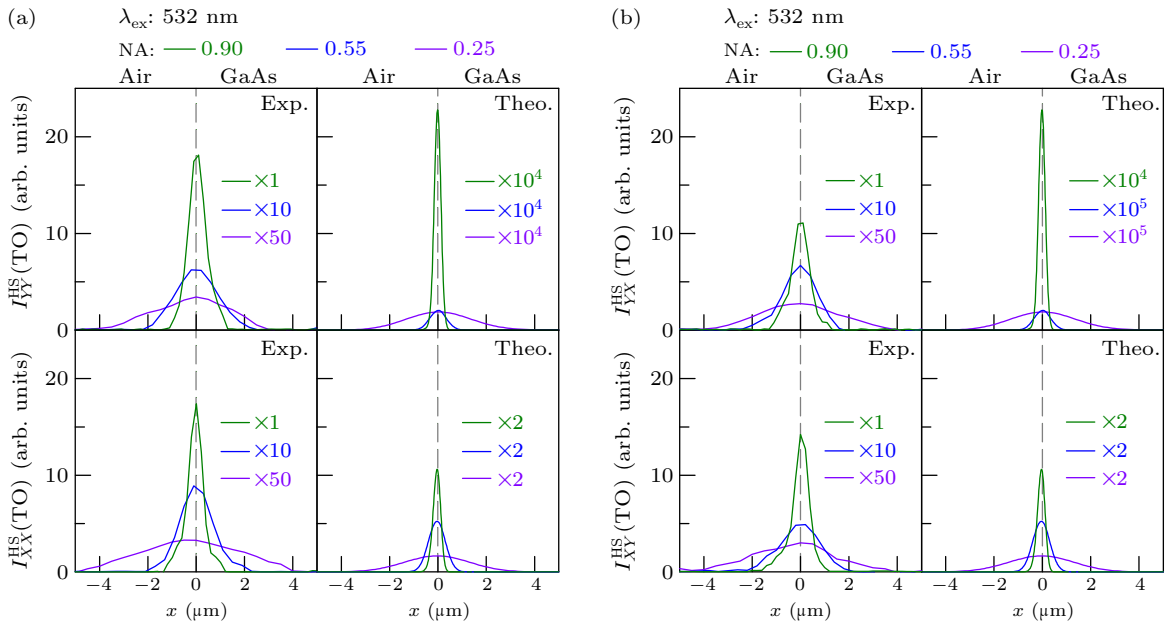



**Fig. 7.** Experimental (Exp.) and theoretical (Theo.) (a) $I_{YY}^{HS}(TO)$ and $I_{XX}^{HS}(TO)$, and (b) $I_{YX}^{HS}(TO)$ and $I_{XY}^{HS}(TO)$ as functions of $x$ excited by $\lambda_{ex} = 532$ nm, NA = 0.90 (green lines), 0.55 (blue lines) and 0.25 (purple lines).

## 4. Conclusion

In conclusion, we employed polarization-resolved Raman spectroscopy to investigate the Raman scattering at the GaAs edge. The enhancement of Raman-active modes and the emergence of Raman-forbidden modes were observed at the edge using varying $\lambda_{ex}$ and objectives with different NAs. The FDTD simulations demonstrate that (i) the edge structure can significantly modify the propagation and distribution of the electromagnetic field of the incident laser, forming a hot spot near the edge; (ii) the $E_Y^Y$ and $E_Y^Z$ ($E_X^X$ and $E_X^Z$) components of the $Y$-polarized ($X$-polarized) incident laser are greatly enhanced at the hot spot; (iii) the modulation for the electromagnetic filed near the edge is dependent on the polarization vector of the incident laser. The theoretical results show strong agreement with experimental data. Our findings can be extended to other semiconductor materials, offering a pathway for innovative applications in the characterization of edge structure and the optimization of photonic devices.

## Acknowledgments

Project supported by the National Key Research and Development Program of China (Grant No. 2023YFA1407000), the Strategic Priority Research Program of Chinese Academy of Sciences (Grant No. XDB0460000), the National Natural Science Foundation of China (Grant Nos. 12322401, 12127807, and 12393832), CAS Key Research Program of Frontier Sciences (Grant No. ZDBS-LY-SLH004), Beijing Nova Program (Grant No. 20230484301), Youth Innovation Promotion Association, Chinese Academy of Sciences (Grant No. 2023125), and CAS Project for Young Scientists in Basic Research (Grant No. YSBR-026).

## References

[1] Son Y W, Cohen M L and Louie S G 2006 *Nature* **444** 347
[2] Yazyev O V 2010 *Rep. Prog. Phys.* **73** 056501
[3] Sepioni M, Nair R, Rablen S, Narayanan J, Tuna F, Winpenny R, Geim A and Grigorieva I 2010 *Phys. Rev. Lett.* **105** 207205
[4] Tang S, Zhang C, Wong D, *et al*. 2017 *Nat. Phys.* **13** 683
[5] Yin X, Ye Z, Chenet D A, Ye Y, O'Brien K, Hone J C and Zhang X 2014 *Science* **344** 488
[6] Candussio S, Durnev M V, Tarasenko S A, Yin J, Keil J, Yang Y, Son S K, Mishchenko A, Plank H, Bel'kov V V, Slizovskiy S, Fal'ko V and Ganichev S D 2020 *Phys. Rev. B* **102** 045406
[7] Ma Q, Lui C H, Song J C W, Lin Y, Kong J F, Cao Y, Dinh T H, Nair N L, Fang W, Watanabe K, Taniguchi T, Xu S Y, Kong J, Palacios T, Gedik N, Gabor N M and Jarillo-Herrero P 2019 *Nat. Nanotech.* **14** 145
[8] Wang Q, Zheng J, He Y, Cao J, Liu X, Wang M, Ma J, Lai J, Lu H, Jia S, Yan D, Shi Y, Duan J, Han J, Xiao W, Chen J H, Sun K, Yao Y and Sun D 2019 *Nat. Commun.* **10** 5736
[9] Tan P H 2019 *Raman Spectroscopy of Two-Dimensional Materials* (Singapore: Springer)
[10] Tan P H, Wu J B, Han W P, Zhao W J, Zhang X, Wang H and Wang Y F 2014 *Phys. Rev. B* **89** 235404
[11] Zhang X, Li Q Q, Han W P, Lu Y, Shi W, Wu J B, Mikhaylushkin A S and Tan P H 2014 *Nanoscale* **6** 7519
[12] Wu J B, Lin M L, Cong X, Liu H N and Tan P H 2018 *Chem. Soc. Rev.* **47** 1822
[13] Xu W, Sun S, Yang M, Hao Z, Gao L, Lu J, Zhu J, Chen J and Cai J 2023 *Chin. Phys. B* **32** 046803
[14] Wolf I D 1996 *Semicond. Sci. Technol.* **11** 139
[15] Mcnally P J, Curley J W, Bolt M, Reader A, Tuomi T, Rantama"ki R, Danilewsky A N and DeWolf I 1999 *J. Mater. Sci.: Mater. Electron.* **10** 351
[16] De Wolf I, Maes H E and Jones S K 1996 *J. Appl. Phys.* **79** 7148
[17] Krishna R, Jones A N, Edge R and Marsden B J 2015 *Radiat. Phys. Chem.* **111** 14
[18] Cançado L G, Pimenta M A, Neves B R A, Dantas M S S and Jorio A 2004 *Phys. Rev. Lett.* **93** 247401
[19] Li Q Q, Zhang X, Han W P, Lu Y, Shi W, Wu J B and Tan P H 2015 *Carbon* **85** 221
[20] Ribeiro H B, Villegas C E P, Bahamon D A, Muraca D, Castro Neto A H, de Souza E a T, Rocha A R, Pimenta M A and de Matos C J S 2016 *Nat. Commun.* **7** 12191
[21] Angulo A M, Noguez C and Schatz G C 2011 *J. Phys. Chem. Lett.* **2** 1978
[22] Abdulhalim I 2018 *Nanophotonics* **7** 1891
[23] Zong C, Xu M, Xu L J, Wei T, Ma X, Zheng X S, Hu R and Ren B 2018 *Chem. Rev.* **118** 4946
[24] Wang X, Huang S C, Hu S, Yan S and Ren B 2020 *Nat. Rev. Phys.* **2** 253
[25] Li C and Jin Y 2021 *Adv. Funct. Mater.* **31** 2008031
[26] Zhang X L, Zhang J, Luo Y and Ran J 2022 *Chin. Phys. B* **31** 077401
[27] Khorasaninejad M, Walia J and Saini S S 2013 *Appl. Phys. Lett.* **103** 163110
[28] Poborchii V, Tada T and Kanayama T 2009 *Appl. Phys. Lett.* **94** 131907
[29] Guo Y, Zhang W, Wu H, Han J, Zhang Y, Lin S, Liu C, Xu K, Qiao J, Ji W, Chen Q, Gao S, Zhang W, Zhang X and Chai Y 2018 *Sci. Adv.* **4** eaau6252
[30] Ribeiro H, Ramos S, Seixas L, De Matos C and Pimenta M 2019 *Phys. Rev. B* **100** 094301
[31] Zhao Y, Zheng L, Han S, Xu B, Fang Z, Zhang J and Tong L 2022 *Nano Res.* **15** 6416
[32] Ribeiro H, Villegas C, Bahamon D, Muraca D, Castro Neto A, De Souza E, Rocha A, Pimenta M and De Matos C 2016 *Nat. Commun.* **7** 12191
[33] Aspnes D E, Kelso S M, Logan R A and Bhat R 1986 *J. Appl. Phys.* **60** 754
[34] Loudon R 1964 *Adv. Phys.* **13** 423
[35] Le Ru E C and Etchegoin P G 2006 *Chem. Phys. Lett.* **423** 63
[36] Yoshida K i, Itoh T, Tamaru H, Biju V, Ishikawa M and Ozaki Y 2010 *Phys. Rev. B* **81** 115406
[37] Ding S Y, Yi J, Li J F, Ren B, Wu D Y, Panneerselvam R and Tian Z Q 2016 *Nat. Rev. Mater.* **1** 16021